Analysis of methods and approaches of the electromagnetic calculation of induction machines regarding their use to solve multiphysical problems

Received 16 July 2021
Revised 29 November 2021
Accepted 30 December 2021

Martin Marco Nell, Marius Franck and Kay Hameyer
Institute of Electrical Machines, RWTH Aachen University, Aachen, Germany

Abstract

Purpose – For the electromagnetic simulation of electrical machines, models with different ranges of values, levels of detail and accuracies are used. In this paper, numerical and two analytical models of an induction machine (IM) are analysed with respect to these aspects. The purpose of the paper is to use these analyses to discuss the suitability of the models for the simulation of various physical quantities of an IM.

Design/methodology/approach – An exemplary IM is simulated using the two-dimensional numerical finite element method, an analytical harmonic wave model (HWM) and an extended HWM. The simulation results are analyzed among themselves in terms of their level of detail and accuracy. Furthermore, the results of operating map simulations are compared with measured operating maps of the exemplary machine, and the accuracy of the simulation approaches is discussed in the context of measurement deviations and uncertainties.

Findings – The difference in the accuracy of the machine models depends on the physical quantity of interest. Therefore, the choice of the simulation method depends on the nature of the problem and the expected range of results. For modeling global machine quantities, such as mean torque or losses, analytical methods such as the HWM s are sufficient in many applications because the simulation results are within the range of measurement accuracy of current measurement systems. Analytical methods are also suitable for local flux density curves under certain conditions. However, for the simulation of the influence of local physical effects on the machine behavior and of temporally highly resolved quantities in saturated operating points, the accuracy of the analytical models decreases and the use of the finite element method becomes necessary.

Originality/value – In this paper, an extension of the HWM is used to calculate the IM, which, in contrast to the HWM, models the saturation. Furthermore, the simulation results of the different electromagnetic IM models are put into the context of the uncertainty of a measurement of several identical IMs.

Keywords Multiphysical problems, Induction machine, Finite element method, Analytic machine modeling

Paper type Research paper

1. Introduction

The modeling, calculation and simulation of electrical machines are described in many publications of research and science. The aim of modeling and calculation is to consider all physical effects that are relevant for the application. The individual physical effects can be

This paper is dedicated to the lifetime work of Professor Andrzej Demenko and Professor Lech Nowak in recognition of their contributions in the field of Electrical Machines.

COMPEL - The international journal for computation and mathematics in electrical and electronic engineering

0332-1649
DOI 10.1108/COMPEL-07-2021-0249

assigned to different physical domains, such as the mechanical, electrical, magnetic and thermal domains. Complex tasks in the field of electrical machines include usually several of these physical domains, and thus, form a multiphysical problem. In such a multiphysical problem, the individual domains can be independent of each other or coupled together. One of the most common examples of coupled domains in electrical machine calculation and simulation is the coupling of the electrical and magnetic domains in electromagnetism.

For the solution of multiphysical problems in the area of electrical machines, a wide variety of technical and scientific fields such as electrical engineering, mechanics, thermodynamics, material sciences, physics, chemistry or mathematics have to be considered. The multiphysical problem can be separated into the question itself and boundary conditions which further define, limit or simplify the problem. Such boundary conditions include requirements for the solution of the problem and limitations or definitions of the physical effects that have to be considered. Thus, these boundary conditions define the level of detail of the multiphysical and coupled problem. In addition to the dependency of the level of detail on those boundary conditions, there is also a dependency on the development status of the system or application, respectively, on the system components and on the expectation of the result. Therefore, depending on the level of detail, different models and approaches can be used to solve multiphysical and coupled problems. The individual models differ in their complexity, their level of detail, their ability to depict physical effects and their computational or solution effort. In the electromagnetic calculation of electric machines empirical models, numerical models (von Pfingsten *et al.*, 2017), lumped parameter models (Boglietti *et al.*, 2008a, 2008b), and analytical models (Li *et al.*, 2018; Oberretl, 1970; Oberretl, 2007; Pugsley *et al.*, 2003) are used.

In this paper, different models and approaches for the electromagnetic calculation and simulation of induction machines (IMs) are analyzed regarding their ability to depict the physical effects of different domains, their level of detail and their accuracy. To evaluate the accuracy, the results of the models are compared with each other and with measurements of an exemplary machine. Thus, the model accuracy is evaluated in the context of the measurement accuracy of a state-of-the-art test bench. The structure of the paper is as follows. First of all, three different modeling methods and approaches, the numerical finite element (FE)-simulation, the analytical calculation using a harmonic wave model (HWM) and the calculation using an extended HWM (E-HWM) to consider saturation, are introduced and analyzed with respect to the mentioned aspects in Section 2. Second, the exemplary IM and the test bench measurement are introduced in Section 3. Finally, simulations are performed with the presented IM models, and the results are compared with each other and with the measurement results in Section 4.

2. Used electromagnetic models of the induction machine

2.1 Finite element model

The first calculation method of the IM considered in this paper is the numerical two-dimensional (2D) transient FE method (T-FEM). The method is described in von Pfingsten *et al.*(2017), and the approach to calculate the entire operating range of the IM using the FEM is depicted in Nell *et al.*(2019a, 2019b) and von Pfingsten *et al.* (2018).

2.1.1 Physical domains and effects. The use of the FEM leads to the possibility to map and model many physical domains and effects. In the 2D-FEM, the physical and magnetic domains are strongly coupled and described by Maxwell's equations. 2D effects like the current displacement effect in the rotor (Carbonieri and Bianchi, 2020) and stator winding (Chin *et al.*, 2018), leakage effects, magnetic saturation, magnetic isotropy and anisotropy and slotting effects can be numerically modeled accurately. Moreover, it is possible to

consider further effects from other domains. In FE models, effects of the mechanical domain, such as mechanical stress in the material, can be coupled with the electromagnetic domain, as it is done in Karthaus *et al.* (2019). Also, cutting edges effects (Elfgen *et al.*, 2015) can be modeled using this numerical method. Furthermore, mechanical, electrical and magnetic asymmetries like eccentricities (Tenhunen, 2001) can be modeled. Three-dimensional effects such as winding head leakage can only be modeled in 2D FEM by additional factors and not in the FEM itself. For this purpose, a three-dimensional FE simulation is necessary.

2.1.2 Level of detail. Based on the calculation of the machine by solving differential equations in every element of the FE mesh, it is possible to locally resolve electromagnetic effects. Solving the FE mesh for several small-time steps means that the temporal distribution of the electromagnetic effects can also be highly resolved. The machine quantities like fluxes, magnetic flux density, torque and also iron losses can be resolved very precisely in space and time. The disadvantage of high spatial and temporal resolution is a high computational effort due to a large number of elements in the mesh and the required simulation time steps. For solving multiphysical problems, the compromise of a quite accurate calculation of the interesting effects and the simulation effort can be of great importance.

2.1.3 Harmonic wave model and extended harmonic wave model. The HWM used in this work was presented by Oberretl (2007, 1970). The HWM uses analytical formulations and the permeance model described in Oberretl (1973), Zhu and Howe (1993) to calculate analytically several machine quantities like the stator and rotor voltages and currents, the torque or the air gap flux density under the influence of the multiple armature reaction and the stator and rotor slotting. It is, thus, able to map the harmonics occurring in the IM. The harmonic model described in Oberretl (2007, 1970) is subject to the assumption of infinite permeability ($\mu \to \infty$) of the rotor and stator laminations. This assumption leads to the fact that Oberretl's model loses its validity in case of saturation of the magnetic circuit.

In the case of saturation, the air gap flux density, which is important for the calculation of the electromagnetic forces, deviates more and more from the sinusoidal curve and flattens out. To model this effect, a description of an effective air gap dependent on the circumferential location Θ is introduced in the E-HWM. As a result of the main field saturation, the air gap is increased on average by a saturation factor $k_h > 1$. In the region of large iron saturation, i.e. at the maximum of the air gap flux density B_δ, the air gap is increased by a further saturation factor k_{h1} and reduced in the zero-crossing of the air gap flux density. This results in the time- and location-dependent air gap conductance function:

$$\lambda(\Theta,\ t) = \frac{1}{k_\mathrm{h}} - \frac{1}{k_\mathrm{h1}} \cdot \cos\left(\frac{2\pi\Theta}{\tau_\mathrm{p}} - 2\omega t\right), \tag{3}$$

where ω is the angular frequency of the magnetic field, τ_p is the pole pitch, and t is the actual time point. Factor two in the cosine argument is a consequence of the simultaneous iron saturation by the north and south poles of the airgap field.

The flattened air gap flux density $B_{\delta,\mathrm{sat}}(\Theta, t)$ follows from the multiplication of the air gap flux density $B_\delta(\Theta, t)$ of the HWM and the air gap conductance function $\lambda(\Theta, t)$ to:

$$B_{\delta,\mathrm{sat}}(\Theta,\ t) = B_\delta(\Theta, t) \cdot \lambda(\Theta, t). \tag{4}$$

The saturation in the trajectories of the mean tooth and yoke flux densities of the HWM can also be accounted for by multiplying the air gap conductance function. The change in the flux densities results in new induced currents in the rotor. These require an iterative

adaptation in the E-HWM. Based on the scaled flux densities, the rotor current is updated, which changes the flux densities, which, in turn, are scaled with the air gap conductance function. In the E-HWM, the induced rotor current is updated by scaling the inductances used to calculate the current using the scaling factor:

$$s_{\mathrm{Ind}} = \frac{1}{k_{\mathrm{h}}}. \tag{5}$$

More details describing the E-HWM model are presented in Nell *et al.* (2021).

2.2 Physical domains and effects

The HWM and E-HWM are able to model effects like slotting effects, the influence of current and voltage harmonics or the multiple armature reaction. The effect of current displacement in the rotor and stator winding as well as leakage effects, such as slot leakage, can be considered by analytical formulas. Furthermore, asymmetries like eccentricities can be modeled with the HWM, as shown in Schröder *et al.* (2015). Not considered are three-dimensional effects and local effects such as the cutting-edge effect or the local influence of mechanical stress on the material properties and the machine's losses.

2.3 Level of detail

Machine quantities like the torque and the air gap flux density can be calculated with the HWM and E-HWM quite accurately in space and time and are less computationally intensive compared to the FEM. The calculation of local field or loss distributions as in the FEM is only possible to a limited extent with the HWM and E-HWM. For example, it is not possible to calculate the flux densities in individual stator and rotor lamination positions. Instead, the mean stator flux and rotor flux in the teeth and yokes are calculated. These correspond approximately to the time flux densities occurring at points $P_{\mathrm{S,T}}$, $P_{\mathrm{S,Y}}$, $P_{\mathrm{R,T}}$ and $P_{\mathrm{R,Y}}$ in Figure 1. For this reason, in contrast to the T-FEM, the iron losses in the HWM and E-HWM cannot be resolved locally. Therefore, to calculate the iron losses in these models, the resulting average iron loss density of the teeth and yokes is calculated using the average tooth and yoke flux densities. By multiplying the average loss densities by the masses of the

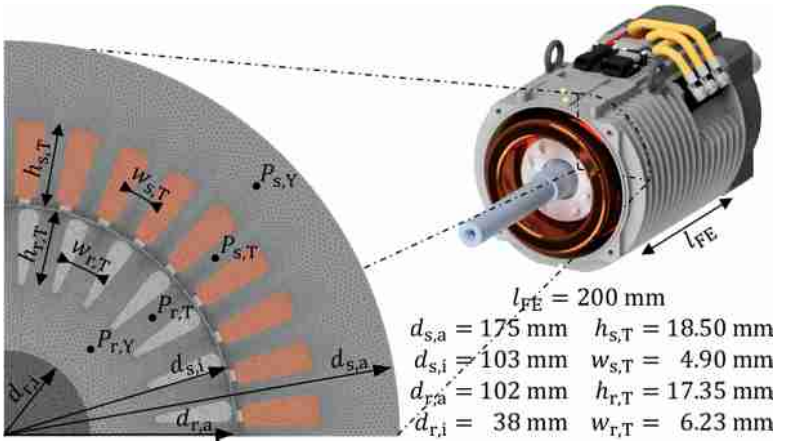

Figure 1.
The exemplary IM and its stator and rotor cross-sectional area

teeth and yokes, the iron losses can be estimated. A detailed explanation of the used iron loss model in all models is conducted in Section 3.1.1.

For linear and high permeable rotor and stator materials where saturation does not occur, the HWM is able to model the mentioned machine variables quite accurately compared to the FEM. For low permeable rotor and stator materials that are subject to the saturation effect, the HWM loses its validity. By using the E-HWM, this disadvantage of the HWM can be reduced. Both aspects are shown in detail in the comparison of the simulation results of the HWM and E-HWM to the T-FEM.

3. Model analysis based on measurements and simulations

For the analysis of the level of detail of each electromagnetic IM model, simulations of an exemplary IM are performed for each model. The simulation results are compared with each other. In addition, the exemplary IM is measured on the test bench, and a comparison of the measurement and simulation results is performed.

3.1 The exemplary induction machine

For the measurements and simulations in this paper an exemplary three phase winding squirrel cage IM with a peak power of $P_{max} = 35$ kW and a rated power of $P_{S2\text{-}30min} = 20$ kW is used. The IM was designed as a traction drive for small electric vehicles and has a rated line to line voltage of $V_{LL,N} = 90$ V and a rated line current of $I_N = 194$ A. It is rated speed is $n_N = 3{,}000$ rpm, and it is maximum speed is $n_N = 8{,}000$ rpm. The rated torque of the IM is $T_N = 64$ Nm, and the maximum torque $T_{max} = 130$ Nm. The IM has an aluminum squirrel cage, a magnetic length of $l_{Fe} = 200$ mm, an outer stator diameter of $d_{s,a} = 175$ mm and a bore diameter of $d_{s,i} = 103$ mm. The IM, its stator and rotor cross-section areas and further data are shown in Figure 1. The IM has a number of pole pairs of $p = 2$ and a number of slots per pole and phase of $q = 3$. The winding is connected in delta connection. It has two parallel winding paths and is not chorded. The rotors of the machines have 28 deep rotor bars. The stator and rotor are constructed from laminated M400-50A steel sheets. The housing is an aluminum cast with cooling fins, and the machine is cooled by a forced flow of air tangentially around the cooling fins. For the measurement, 10 of these machines were used. They have been extracted from two series production batches with five individual machines in each batch.

3.2 Test bench measurements

To analyze the results of the different methods and approaches of the electromagnetic calculation of an IM and to compare them with measurements, the example machines are measured on a machine test bench. For the measurements, the test bench setup described in von Pfingsten *et al.* (2017) is used. An HBM T12 torque transducer with a specified accuracy of 0.03% is used for torque and speed measurements. The three-phase currents of the machines are measured with a two-stage measurement setup. A LEM IT 400-S ULTRASTAB current transformer reduces the currents by a factor of 2,000, and the reduced phase currents are then measured using a YOKOGAWA WT3000 precision power analyzer. The voltages are measured using a voltage measurement system from the Institute of Electrical Machines (IEM) in combination with the YOKOGAWA WT3000. For the measurements, the IMs were operated with a dc link voltage of $V_{dc} = 130$ V and a maximum inverter current of $I_{inv,max} = 355$ A. An inverter with a switching frequency of 10 kHz is used. The influence of the inverter circuit on the losses of the machine was analyzed. By adding a low-pass filter to the power analyzer and comparing the measured electrical input power with and without low-pass filtering of the input voltages and currents, the influence

of inverter switching on the machine losses was considered. The influence was measured to be less than 20 W. Therefore, the switching losses are not considered in the simulation. The IMs are controlled by means of a field-oriented control in which the ohmic losses of the machine are minimized. For thermal monitoring and analysis, the winding temperatures $\vartheta_{\mathrm{Winding}}$ are measured at seven different locations in the stator winding system. A non-contact infrared (IR) temperature measurement on the surface of the shorting ring is used to measure the rotor temperature ϑ_{r}. The rotor surface is sprayed black to create a nonreflective surface in the IR region, i.e. an IR emissivity > 0.97 (von Pfingsten *et al.*, 2017). For each of the 10 IMs the stator currents I_{S}, the stator voltages V_{S}, the electrical input power P_{el}, the speed n, the torque T, the mechanical power P_{mech}, the power factor cos (φ) and the stator current frequency f_{S} for the entire operating range is measured. The measurement points are discretized in speed steps of Δn = 500 rpm and torque steps of ΔT = 10 Nm. Each operating point is measured at a nearly constant stator winding temperature of $\vartheta_{\mathrm{winding}}$ = 80°C and a rotor temperature of ϑ_{R} = 100°C. The machines were conditioned to these temperatures between the individual measurements of each operating point.

3.2.1 Measurement results of the different machines. Because direct measurement of the machine losses is not possible, it is determined from the measured input and output powers. The losses of the IM are, thus, the difference between the measured output power of the inverter minus the ohmic losses in the motor supply cables and the measured mechanical output power. By using the measured stator resistance R_{S} of the IM these losses can be divided into stator ohmic losses and all other losses. A further loss separation is not possible with this test setup. Because the mentioned quantities are measured for all 10 IMs the mean value over the 10 machines for each quantity is calculated and builds the basis of the comparisons with the calculation methods and approaches. In Figure 2(a), the averaged losses of the measuring machine in the entire operating range are shown. Each individual

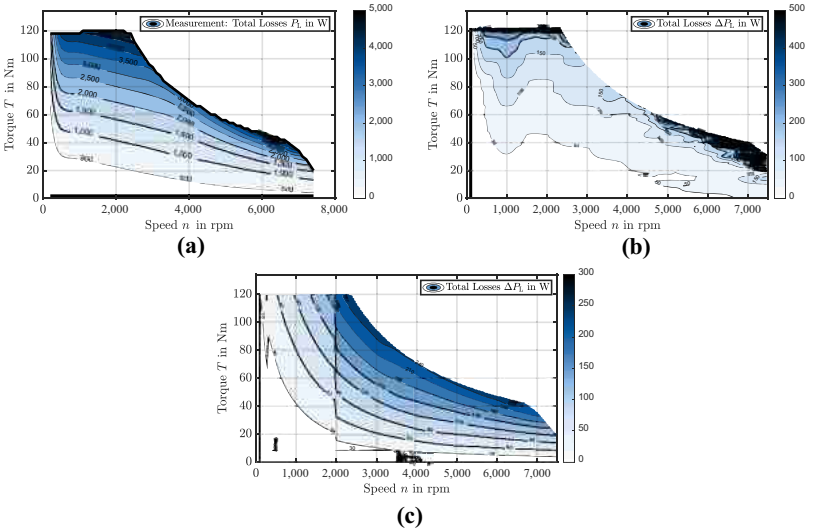

Figure 2.
Measured mean losses of the exemplary IM (a), maximum loss deviation of the total losses between the measured IM (b) and calculated loss power deviation due to measurement uncertainties (c)

machine shows a slightly different efficiency, and therefore, has a slightly different loss power. The reason for this can be production deviations because of tolerance deviations, measurement uncertainties, and the accuracy of the measurement equipment. In Figure 2(b), the maximum difference of the measured loss power of the 10 machines is shown. The difference in the measured losses reaches values up to $\Delta P_L = 200$ W.

3.2.1.1 Measurement accuracy. The accuracy of a measured machine quantity is dependent on the accuracy of the measurement equipment and the operating point. To quantify the accuracy of the measurement, the theoretical maximum errors that are specified in the datasheets of the measuring instruments are used. For example, the accuracy of the HBM T12 speed measurement is 150 ppm resulting in a maximum absolute speed error of $\Delta n = 1.8$ rpm referred to the maximum speed of $n = 12{,}000$ rpm, and the accuracy of the torque transducer is 0.03%. The accuracy of the voltage measurement device of the IEM is 0.2%. Due to the series connection of individual measuring devices, the relative errors add up. For the calculation of machine values y, such as the loss power P_L, out of the measured quantities x_i, the uncertainties of the measured quantities $u(x_i)$ are used to determine the combined standard uncertainty:

$$u_c(y) = \sum_{i=1}^{N} \left(\frac{\partial f}{\partial x_i} \right)^2 u^2(x_i) \tag{1}$$

where f is the function used to calculate the output value $y = f(x_1, x_2, \ldots, x_N)$. The calculation is performed according to the guide to the expression of uncertainty in measurement. The uncertainty of the measured losses of the IM according to the presented calculation approach is shown in Figure 2(c).

3.3 Simulation of the exemplary induction machine

3.3.1 Simulation settings. The geometry of the example machine shown in Figure 1 is used to simulate the machine. The simulations are performed with the HWM, the E-HWM and the T-FEM. The T-FEM simulation is performed both with the magnetic properties of the M400-50 A steel sheets and with a constant high permeability of the stator and rotor of $\mu_r = 10{,}000$. By simulating with the permeability of $\mu_r = 10{,}000$, there are no saturation effects in the simulation, and the T-FEM results can be compared with the results of the HWM. The T-FEM simulation is a current-driven simulation in which the stator slots are excited with a sinusoidal current density. The simulations are performed in the stator current and rotor current frequency map (I_S-f_R-map) or stator slot current density and rotor current frequency map ($J_{S,Slot}$-f_2-map), respectively at a constant stator frequency of $f_S = 86$ Hz. To generate the speed-torque map (T-n-map), the results in the I_S-f_R-map are transformed into the T-n-map. For each speed-torque operating point, the I_S-f_R-operating point with the lowest ohmic losses is determined. Frequency-dependent losses such as the iron losses are scaled according to the speed or stator fundamental frequency. A detailed explanation of this simulation principle can be found in von Pfingsten *et al.* (2018). For the exemplary IM, 14 equidistant stator slot current densities from $J_{S,Slot} = 0$ A/mm^2 up to $J_{S,Slot} = 13$ A/mm^2 and 15 equidistant rotor current frequencies from $f_R = 0$ Hz to $f_R = 16$ Hz are simulated in the $J_{S,Slot}$-f_2- map. The temporal sampling is 100 μs in all simulations, which corresponds to a sampling frequency of $f_{samp} = 10$ kHz.

The losses due to the current displacement effect in the stator winding are estimated in the models by an analytical calculation according to Bauer *et al.* (2015), Joksimovic and Binder (2004). The current displacement effect in the rotor bars is considered in the T-FEM

simulation by calculating the rotor current density in each element of the rotor bar and in the HWM and E-HWM by using an analytical current displacement factor (Oberretl, 1973), analogous to the current displacement of the stator winding. The mechanical friction losses were measured on the test bench by driving the device of the test and considered in the simulation as a loss torque. Slot leakage in the stator and rotor are considered in the analytical models by means of leakage factors, according to (Boglietti *et al.*, 2008a; Oberretl, 1973). The iron losses are calculated using the IEM-5 parameter formula (Steentjes *et al.*, 2013a):

$$P_{\mathrm{Fe,IEM}} = a_1 \; B_{\mathrm{m}}^{\alpha B_{\mathrm{m}}} \; f + a_2 \; B_{\mathrm{m}}^2 \; f^2 + a_5 B_{\mathrm{m}}^{1.5} \; f^{1.5} + \; a_2 \; a_3 \; B_{\mathrm{m}}^{a_4+2} \; f^2, \tag{2}$$

where f is the frequency B_{m} the flux density, a_1, a_2 and a_5 are the hysteresis, eddy current and excess loss factors, a_2 and a_4 are loss parameters describing the nonlinear saturation losses, and α is the exponent of the hysteresis losses. The model is validated in (Steentjes *et al.*, 2013b). To calculate the iron losses in the T-FEM, the flux density in each element is decomposed into its spectral components by means of a Fourier transformation and the IEM-5-parameter formula is applied to the individual spectral components. The flux density is first decomposed into radial and tangential flux density components. The total iron losses are then obtained from the iron loss densities of all elements and the determined masses of the stator and rotor. In the HWM and E-HWM, the evaluation of the iron losses cannot be carried out in individual positions of the stator and rotor, as already mentioned. Therefore, the IEM-5-parameter formula is applied only to the frequency spectra of the averaged tooth and yoke flux densities. A more detailed description of this method for the iron loss calculation in the FEM is given in von Pfingsten *et al.*(2016). The loss parameters of the M400-50A material for the simulation are determined by measurement and listed in Table 1. The same parameters were assumed for the linear simulation. The method of metrological determination of the parameters is described in (Steentjes *et al.*, 2013b). To assess the computational effort, the degrees of freedom of the models are analyzed. For the T-FEM, the degrees of freedom consists of the number of operating points, the nodes in the mesh, the numerical iterations and the transient steps. In the HWM, they are also described by the number of operating points and, in addition, by the stator and rotor orders considered as well as the Fourier coefficients of the stator and rotor permeance functions. In the E-HWM, the iterations for updating the rotor current are added. In the simulations carried out, a degree of freedom lower by a factor of 120 results for the E-HWM and a degree of freedom lower by a factor of 350 for the HWM compared with the T-FEM.

3.3.2 Simulation results. In the following, the simulations of the T-FEM, the HWM and the E-HWM are compared with the measurement. The stator currents, the rotor current frequency and the total losses are analyzed within the T-n-map. Because in the measurement, a further separation of the losses into ohmic rotor losses and iron losses is not possible, these quantities are only compared under the simulations. Figure 3(a) compares the stator phase currents I_{S} and Figure 3(b) the rotor current frequencies f_{R} of the measurement and the simulations. The T-n-maps were calculated using the method described above. It

Table 1.
Iron loss parameter used in the simulation of the exemplary IM

a_1	a_2	a_3	a_4	a_5	$a_{1,90°}$	$a_{5,90°}$	α
0.0231	$1.2718 \cdot 10^{-4}$	0.1486	3.0583	0.0004	–	–	1.6217

can be seen that for both the stator current and the rotor current frequency, the T-FEM provides the best results compared with the measurement. The E-HWM deviates more strongly from the measurement results than the T-FEM, especially in areas of high saturation, which are reached at high currents. The HWM also shows good agreement with the measurement in the linear range, i.e. at low stator currents. In the range of higher currents, the strong limitation of the HWM becomes apparent, and the deviations become very large. In particular, the rotor current frequency shows a clearly different curve. This is due to the fact that for the given speed torque operating points due to the neglect of saturation in the HWM, the operating points of minimum ohmic losses in the I_S-f_R-map deviate strongly from those of the other models and the measurement. The results are also reflected in the total losses, rotor ohmic losses and iron losses. Figure 3(c) shows the simulated rotor ohmic losses, and Figure 3(d) shows the iron losses. The E-HWM approximates the iron losses quite well compared with the T-FEM despite the neglect of local iron loss distributions.

In Figure 4, the differences of the measured to the simulated total losses are plotted. Again, the results with the T-FEM are the most accurate. The deviations are in the range of $\Delta P_L = 0\,W$ to $\Delta P_L = 150\,W$ and within the measurement deviations of the individual machines in Figure 2(b) and the calculated measurement accuracies in Figure 2(c). For the E-HWM, the deviations are with $\Delta P_L = 0\,W$ to $\Delta P_L = 300\,W$, slightly larger, but also within the measurement deviations and measurement accuracies. The losses simulated with the HWM show very large deviations, especially in the areas of higher saturation with differences of more than $\Delta PL = 300\,W$.

For a closer examination of the differences between the T-FEM and the HWM or E-HWM, the simulated air gap flux densities and stator tooth flux densities are compared for a linear material characteristic with $\mu_r = 10{,}000$ in Figure 5 and for a nonlinear material characteristic given with the M400-50 A steel sheet in Figure 6. A comparison with a measurement in the motor itself cannot be made here. These physical quantities were chosen for analysis because the air gap flux density is the basis for the torque and the electromagnetic forces, and the flux densities in the laminations are the basis for the iron

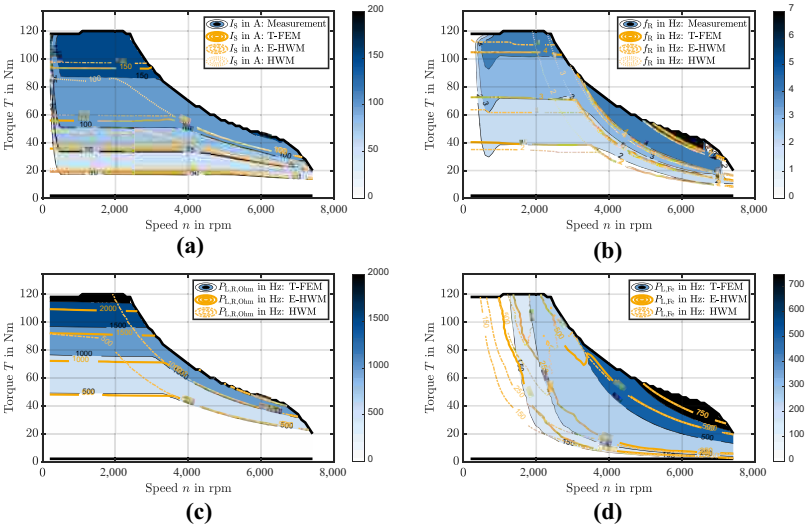

Figure 3.
Measured and simulated stator phase current (a) and rotor current frequency (b) and simulated ohmic rotor losses (c) and iron losses (d) using the T-FEM, E-HWM and HWM

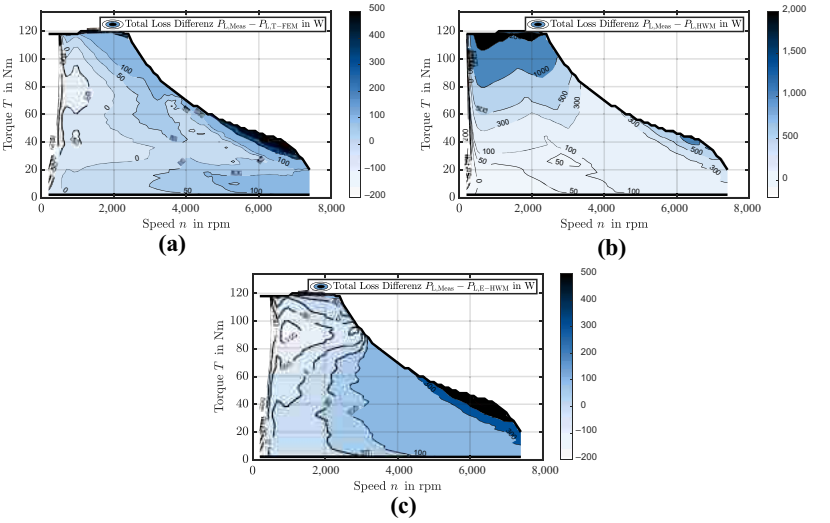

Figure 4.
Difference of measured and simulated total losses for a simulation with the T-FEM (a), the HWM (b) and the E-HWM (c)

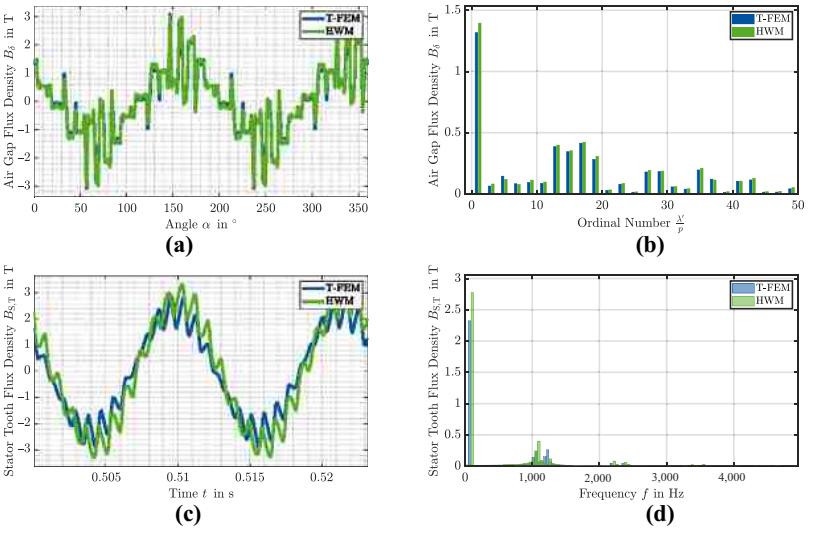

Figure 5.
Air gap flux density (a) and stator tooth flux density (c) and their frequency spectra (b) and (d) simulated with the T-FEM and HWM for a stator and rotor material with a constant permeability of $\mu_{Fe} = 10{,}000$

loss calculation. The operating point is the same for both comparisons. A stator phase current of $I_S = 224.2$ A, a rotor current frequency of $f_R = 4$ Hz and a stator current frequency of $f_S = 86$ Hz are used. The comparison of the HWM with the linear T-FEM shows good agreement in both the time history and frequency spectrum. Therefore, the slotting effects and the multiple armature reaction are accurately represented by the HWM. The stator tooth flux density can also be represented well with the HWM. In the case where iron saturation is considered, the HWM is no longer valid, as can be seen from the comparison of the flux densities in Figure 5 with those of the nonlinear T-FEM simulation in Figure 6. The E-HWM

gives identical results as the HWM in the linear case but can simulate the air gap flux density and stator tooth flux density much more accurately in the nonlinear case. In particular, the basic order is very well represented by the E-HWM with a deviation of $<2\%$. For the higher orders; however, the deviations are larger, which leads to the different time courses in Figure 6(a) and 6(c). This shows that the saturation effect for higher frequency orders in the E-HWM still needs to be improved.

4. Conclusion

In this paper, one numerical and two analytical methods for electromagnetic calculation of IMs are analyzed. The analysis focuses on the physical value ranges, the level of detail and the simulation accuracy. To evaluate the simulation accuracy, an exemplary IM is simulated with each of the mentioned models. In addition, the losses and other machine quantities are measured over the entire operating range of 10 IMs on the test bench, and the measurement deviations and the measurement accuracy are analyzed. The simulation results of the models are compared with each other and with the measured results. The analysis considers both global machine variables, such as the total losses in the torque-speed-map, and local variables, such as the spatial flux density distribution in the air gap and the temporal flux density distribution in the stator tooth of the machine.

The analyses of the global quantities in the IM operating map and the comparison with the measurements show that the T-FEM has the highest accuracy for both unsaturated and saturated operating points. However, the E-HWM is only slightly worse in comparison. Both models provide deviations of the total power loss for the operating range of the exemplary machine compared with the measurement, which is within the determined measurement deviations of the individual measured IMs and the measurement accuracy of current measurement systems. The HWM can fulfill these conditions only in the unsaturated operating points, whereas it leads to very high errors in the saturated ones.

Regarding local physical quantities, a distinction can be made between the local and temporal representation of the air gap flux density and the flux densities in the stator and rotor, respectively. The air gap flux density can be simulated locally and temporally by all

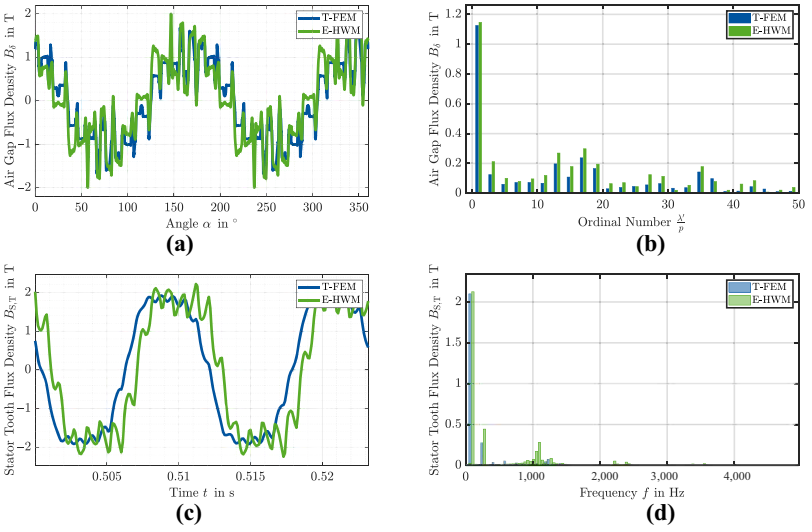

Figure 6.
Air gap flux density (a) and stator tooth flux density (c) and their frequency spectra (b) and (d) simulated with the T-FEM and E-HWM for a stator and rotor material with the magnetic characteristic of an M400-50A steel sheet

models. However, the flux densities in the stator and rotor can only be calculated locally in the T-FEM. In the analytical models, only the mean tooth and yoke flux densities can be determined. Under the condition of a highly permeable stator and rotor material, the air gap flux density is very accurately represented by the HWM than the T-FEM. The orders occurring due to the slotting effect and the multiple armature reaction are well represented. This also applies to the mean tooth and yoke flux densities in the stator and rotor. Under the condition of a stator and rotor with electrical laminations with nonlinear magnetic material behavior, the HWM loses its validity in saturated operating points, which leads to very high deviations from the T-FEM. The E-HWM provides a good agreement of the air gap flux density and tooth and yoke flux densities even in saturated operating points. In particular, the basic order is calculated satisfactorily with deviations below 2% to the T-FEM. The deviations in the higher orders are larger, and therefore, offer the potential to improve the E-HWM for the saturation effect of the higher orders. This means that time histories resulting from the air gap flux density, such as torque and electromagnetic forces, and those resulting from the time histories of the flux densities in the stator and rotor, such as iron losses in the stator tooth, can be simulated in linear operating points by the HWM and E-HWM similarly well as by the T-FEM. With a reduction of the degree of freedom by a factor of more than 100 compared with the T-FEM, the analytical models offer a high saving in computational effort. At nonlinear operating points, on the other hand, only the E-HWM offers an initial rough calculation option for those quantities. The orders of the individual quantities are determined very well, but the amplitudes of the higher orders differ more strongly from those of the T-FEM due to the lower level of detail of the saturation effect. This, thus, has a direct influence on values such as the exciting electromagnetic forces and the noise, vibration and harshness (NVH) behavior, as well as the temperature distribution in the machine. A more detailed analysis of the resulting influence of the different models on the NVH behavior is still pending.

References

Bauer, D., Mamuschkin, P., Reuss, H.-C. and Nolle, E. (2015), "Influence of parallel wire placement on the AC copper losses in electrical machines", *2015 IEEE International Electric Machines and Drives Conference (IEMDC), Coeur d'Alene, ID*, pp. 1247-1253, doi: 10.1109/IEMDC.2015.7409221.

Boglietti, A., Cavagnino, A. and Lazzari, M. (2008a), "Algorithms for the computation of the induction motor equivalent circuit parameters – Part II", *34th Annual Conference of IEEE Industrial Electronics*, pp. 2028-2034, doi: 10.1109/IECON.2008.4758268.

Boglietti, A., Cavagnino, A. and Lazzari, M. (2008b), "Algorithms for the computation of the induction motor equivalent circuit parameters – Part II", *34th Annual Conference of IEEE Industrial Electronics*, pp. 2028-2034, doi: 10.1109/IECON.2008.4758268.

Carbonieri, M. and Bianchi, N. (2020), "Induction motor rotor losses analysis methods using finite element", *2020 IEEE International Conference on Industrial Technology (ICIT)*, pp. 187-192, doi: 10.1109/ICIT45562.2020.9067209.

Chin, J.-W., Jung, Y.-H., Ryu, J.-Y., Park, M.-R. and Lim, M.-S. (2018), "Computationally cost-efficient characteristics analysis of EV traction motor considering AC copper loss based on 2-D magneto-static analysis", *2018 XIII International Conference on Electrical Machines (ICEM), Alexandroupoli, Greece*, pp. 1723-1729, doi: 10.1109/ICEM49940.2020.9271053.

Elfgen, S., Böhmer, S., Steentjes, S., Franck, D. and Hameyer, K. (2015), "Continuous model of magnetic material degradation due to cutting effects in the numerical simulation of electro laminations", *IKMT 2015, 10, ETG/GMM-Symposium Innovative small Drives and Micro-Motor Systems*, pp. 1-6.

Joksimovic, G. and Binder, A. (2004), "Additional no-load losses in inverter-fed high-speed cage induction motors", *Electrical Engineering (Archiv Fur Elektrotechnik)*, Vol. 86 No. 2, pp. 105-116, doi: 10.1007/s00202-003-0185-3.

Karthaus, J., Groschup, B., Krüger, R. and Hameyer, K. (2019), "Mechanical stress distribution and the utilisation of the magneto-elastic effect in electrical machines", *Compel – the International Journal for Computation and Mathematics in Electrical and Electronic Engineering*, Vol. 38 No. 4, pp. 1085-1097, doi: 10.1108/COMPEL-10-2018-0387.

Li, K., Cui, S., Bouscayrol, A. and Hecquet, M. (2018), "Analytical derivation of efficiency map of an induction machine for electric vehicle applications", *2018 IEEE Vehicle Power and Propulsion Conference (VPPC)*, pp. 1-6, 10.1109/VPPC.2018.8605000.

Nell, M., Lenz, J. and Hameyer, K. (2019a), "Scaling laws for the FE solutions of induction machines", *Archives of Electrical Engineering*, Vol. 68 No. 3, pp. 677-695, doi: 10.24425/AEE.2019.129350.

Nell, M., Kubin, A. and Hameyer, K. (2021), "Approach for the model and parameter selection for the calculation of induction machines", *Energies*, Vol. 14 No. 18, p. 5623, doi: 10.3390/en14185623.

Nell, M., Mönninghoff, S., Groschup, B., Müller, F., Karthaus, J., Jaeger, M., Schröder, M., Leuning, N. and Hameyer, K. (2019b), "Complete and accurate modular numerical computation scheme for multi-coupled electric drive systems", *IET Science, Measurement and Technology*, Vol. 14 No. 3, pp. 259-271, doi: 10.1049/iet-smt.2019.0413.

Oberretl, K. (1970), "Field-harmonic theory of slip-ring motor taking multiple armature reaction into account", *Proceedings of the Institution of Electrical Engineers*, Vol. 117 No. 8, pp. 1667-1674, doi: 10.1049/piee.1970.0294.

Oberretl, K. (1973), "Einseitiger linearmotor mit käfig im sekundärteil", *Archiv für Elektrotechnik*, Vol. 56 No. 6, pp. 305-319, doi: 10.1007/BF01459967.

Oberretl, K. (2007), "Losses, torques and magnetic noise in induction motors with static converter supply, taking multiple armature reaction and slot openings into account", *IET Electric Power Applications*, Vol. 1 No. 4, pp. 517-531, doi: 10.1049/iet-epa:20060435.

Pugsley, G., Chillet, C., Fonseca, A. and Bui-Van, A.-L. (2003), "New modeling methodology for induction machine efficiency mapping for hybrid vehicles", *IEEE International Electric Machines and Drives Conference 2003 (IEMDC'03)*, Vol. 2, pp. 776-781, doi: 10.1109/IEMDC.2003.1210324.

Schröder, M., Franck, D. and Hameyer, K. (2015), "Analytical modeling of manufacturing tolerances for surface mounted permanent magnet synchronous machines", *2015 IEEE International Electric Machines and Drives Conference (IEMDC)*, *Coeur d'Alène, ID*, pp. 1138-1144, doi: 10.1109/IEMDC.2015.7409204.

Steentjes, S., Lemann, M. and Hameyer, K. (2013a), "Semi-Physical parameter identification for an iron-loss formula allowing loss-separation", *Journal of Applied Physics*, Vol. 113 No. 17, p. 17A319, doi: 10.1063/1.4795618.

Steentjes, S., von Pfingsten, G., Hombitzer, M. and Hameyer, K. (2013b), "Iron-loss model with consideration of minor loops applied to FE-simulations of electrical machines", *IEEE Transactions on Magnetics*, Vol. 49 No. 7, pp. 3945-3948, doi: 10.1109/TMAG.2013.2244072.

Tenhunen, A. (2001), "Finite-element calculation of unbalanced magnetic pull and circulating current between parallel windings in induction motor with non-uniform eccentric rotor", paper presented at the Electromotion 2001, Bologna, pp. 19-24.

Von Pfingsten, G., Steentjes, S. and Hameyer, K. (2017), "Operating point resolved loss calculation approach in saturated induction machines", *IEEE Transactions on Industrial Electronics*, Vol. 64 No. 3, pp. 2538-2546, doi: 10.1109/TIE.2016.2597761.

Von Pfingsten, G. Ruf, A. Steentjes, S. and Hameyer, K. (2016), "Operation mode dependent requirements on magnetic properties of NO electrical steel in traction drives", ser. Tagungsband – Aachener Stahlkolloquium– Umformtechnik., Verlagshaus Mainz GmbH Aachen, Gerhard Hirt (Hrsg.), no. 1, pp. 163-176.

von Pfingsten, G., Nell, M.M. and Hameyer, K. (2018), "Hybrid simulation approaches for induction machine calculation", *COMPEL – The International Journal for Computation and Mathematics in Electrical and Electronic Engineering*, Vol. 37 No. 5, pp. 1744-1754, doi: 10.1108/COMPEL-01-2018-0015.

Zhu, Z.Q. and Howe, D. (1993), "Instantaneous magnetic field distribution in brushless permanent magnet dc motors. III. effect of stator slotting", *IEEE Transactions on Magnetics*, Vol. 29 No. 1, pp. 143-151, doi: 10.1109/20.195559.

Corresponding author
Martin Marco Nell can be contacted at: martin.nell@iem.rwth-aachen.de